doi: 10.82124/CEAS-GNC-2026-044 CEAS-GNC-2026-044

Cascaded Control Barrier Function Method for Safe Spacecraft Rendezvous

Jonghyun Woo Department of Mechanical Engineering, Chung-Ang University, Seoul, Korea

Yeongho Kim Department of Mechanical Engineering, Chung-Ang University, Seoul, Korea

Namhoon Cho Department of Aerospace Engineering, Seoul National University, Seoul, Korea

Seokwon Lee[†] Department of Mechanical Engineering, Chung-Ang University, Seoul, Korea

ABSTRACT

Safe spacecraft rendezvous requires the chaser to satisfy stringent path constraints during proximity operations while preserving convergence to the docking state. Although high-order control barrier functions (HOCBFs) provide a systematic way to enforce safety, their monolithic constraint at the final control input level can lead to boundary riding behavior and degraded transient performance in path constrained rendezvous scenarios. This paper proposes a cascaded control barrier function (CCBF) framework for safe spacecraft rendezvous. By decomposing the safety constraint into sequential cascade layers, the proposed approach enforces safety consistency from the virtual control level to the actual force input, thereby improving design traceability and tuning tractability compared with conventional HOCBF formulations. The method is applied to satellite rendezvous scenarios subject to a semi-cubical cone path constraint, within a backstepping based sequential control Lyapunov function-quadratic programming (CLF-QP) architecture. Numerical simulation demonstrates that both HOCBF and the proposed CCBF maintain the prescribed safety corridor, whereas the proposed CCBF yields smoother and faster convergence to the docking region with reduced boundary-riding behavior under the same path constraint.

Keywords: Control Barrier Function, Spacecraft Rendezvous, Cascaded Control, Safety-Critical Control

1 Introduction

In the operation of autonomous systems, safety violations can lead to critical system failures or severe threats to public safety [1–3]. Systems that demand safety guarantees are broadly classified as safety-critical systems, encompassing domains such as robotic systems, autonomous vehicles, and aerospace systems. Particularly in the aerospace domain, satisfying critical safety requirements—such as flight envelope protection, geofencing, and collision avoidance—requires operating within highly complex and dynamic environments.

According to recent studies on space missions [4], the position and attitude dynamics of spacecraft are highly coupled, making them challenging to control. Due to the mission complexity of operations such as rendezvous and docking, strict safety guarantees, including collision avoidance and state constraints during the approach to a target, are critical for the survivability of the spacecraft. Approaches such as artificial potential fields (APF) [5, 6] or constrained optimal controllers [7–10] have been utilized to enforce these rigorous safety requirements.

APF methods have been extensively investigated for safe proximity operations. For instance, Shao et al. [5] proposed an APF-based immersion and invariance adaptive pose controller, utilizing Lyapunov's direct method to formally prove the asymptotic stability of the closed-loop system. Wang et al. [6] formulated a convex APF featuring a single global minimum to integrate pyramid-type pose constraints directly into the controller design. Barrier Lyapunov Functions (BLFs) have been widely employed to manage strict state boundaries. Huang et al. [7] incorporated BLFs into a backstepping framework to establish an integrated adaptive finite-time control law for full state constraints. Similarly, Sun et al. [8, 9] leveraged BLF-based backstepping designs to ensure relative state constraints during spacecraft maneuvers. From an optimization-based perspective, Zhou et al. [10] utilized sequential convex programming within a model predictive control (MPC) architecture, translating nonlinear and nonconvex constraints, such as field-of-view limits and complex obstacle regions around the target body, into tractable second-order cone programming sub-problems.

To enforce these rigorous state constraints, a variety of safety filters have been developed to modify nominal control inputs and ensure system safety [11]. Among these approaches, Control Barrier Functions (CBFs) [12] have emerged as an optimization-based mathematical framework. By mapping complex state constraints to the control input space, CBFs enforce the forward invariance of safe sets through quadratic programming (QP) with minimal control modification. Nevertheless, constructing valid CBFs and tuning them for highly complex or cascaded systems is not yet fully established [3]. Furthermore, standard monolithic CBF formulations often struggle to maintain non-conservativeness and theoretical rigor when applied to complex dynamic environments. To address these challenges, we introduce a Cascaded CBF (CCBF) architecture that decomposes safety constraints into sequential layers. Compared to conventional High-Order CBF (HOCBF) formulations [13], this hierarchical structure ensures safety consistency and facilitates the design and tuning processes of the safety filters. The effectiveness of the proposed framework is validated through a path-constrained spacecraft rendezvous and docking scenario [14].

The remainder of this paper is structured as follows. Section 2 provides the mathematical preliminaries and foundational concepts regarding Control Barrier Functions. Section 3 establishes the relative motion dynamics of a chaser spacecraft with respect to a target, which serves as the simulation scenario for validating the proposed methodology. Section 4 details the theoretical formulation of the proposed CCBF architecture. This section mathematically demonstrates how the cascaded framework decomposes spatial boundaries into sequential control layers to guarantee the forward invariance of the safe set. Finally, simulation results and concluding remarks are presented in Section 5.

2 Preliminaries

Safety is formulated as ensuring the forward invariance of a safe set, guaranteeing that the system state does not leave this set. Following existing research [12, 13, 15], consider a state space $\mathcal{X} \subset \mathbb{R}^n$ and a continuously differentiable function $h : \mathcal{X} \to \mathbb{R}$. We define the safe set C, its boundary ∂C, and its interior $\mathrm{Int}(C)$ as follows:

$$\begin{aligned} C &= \{x \in \mathcal{X} : h(x) \geq 0\} \\ \partial C &= \{x \in \mathcal{X} : h(x) = 0\} \\ \mathrm{Int}(C) &= \{x \in \mathcal{X} : h(x) > 0\}. \end{aligned} \tag{1}$$

Definition 1 (*Barrier Function* [12]): The function $h : \mathcal{X} \to \mathbb{R}$ is a barrier function for a continuous-time dynamical system $\dot{x} = f(x)$ if there exists an extended class $\mathcal{K}$ function α such that:

$$\dot{h}(x) + \alpha\left(h(x)\right) \geq 0, \quad \forall x \in \mathcal{X}. \tag{2}$$

Definition 2 (*Control Barrier Function* [12]): Given the safe set C defined in (1), $h(x)$ is a control barrier function for a control-affine system $\dot{x} = f(x) + g(x)u$ if there exists an extended class $\mathcal{K}$ function α such that:

$$\sup_{u \in \mathcal{U}} \left[L_f h(x) + L_g h(x) u + \alpha \left(h(x) \right) \right] \geq 0, \quad \forall x \in \mathcal{X}, \tag{3}$$

where $L_f h(x) \equiv \nabla h(x) f(x)$ and $L_g h(x) \equiv \nabla h(x) g(x)$ denote the Lie derivatives of $h(x)$ along the vector fields f and g, respectively.

Definition 3 (*High-order CBF* [13]): For an m-th order continuously differentiable function $h : \mathcal{X} \to \mathbb{R}$, a sequence of functions $\psi_i : \mathcal{X} \to \mathbb{R}, i \in \{1, \ldots, m\}$ is defined in the form

$$\psi_i(x) = \dot{\psi}_{i-1}(x) + \alpha_i \left(\psi_{i-1}(x) \right), \quad i \in \{1, \ldots, m\} \tag{4}$$

where $\alpha_i(\cdot)$ denotes extended class $\mathcal{K}$ function of their argument and $\psi_0(x) = h(x)$. Then, a sequence of safety set C_i associated with (4) is defined as

$$C_i = \{ x \in \mathcal{X} : \psi_i(x) \geq 0 \}, \quad i \in \{1, \ldots, m\}. \tag{5}$$

A function $h : \mathcal{X} \to \mathbb{R}$ is a high-order control barrier function (HOCBF) of relative degree m for a control affine system if there exist differentiable extended class $\mathcal{K}$ functions $\alpha_i, i \in \{1, \ldots, m\}$ subject to

$$\sup_{u \in \mathcal{U}} \left[L_f^m h(x) + L_g L_f^{m-1} h(x) u + \alpha_m(\psi_{m-1}(x)) \right] \geq 0, \quad \forall x \in C_1 \cap, \ldots, \cap C_m. \tag{6}$$

3 Relative Motion Dynamics

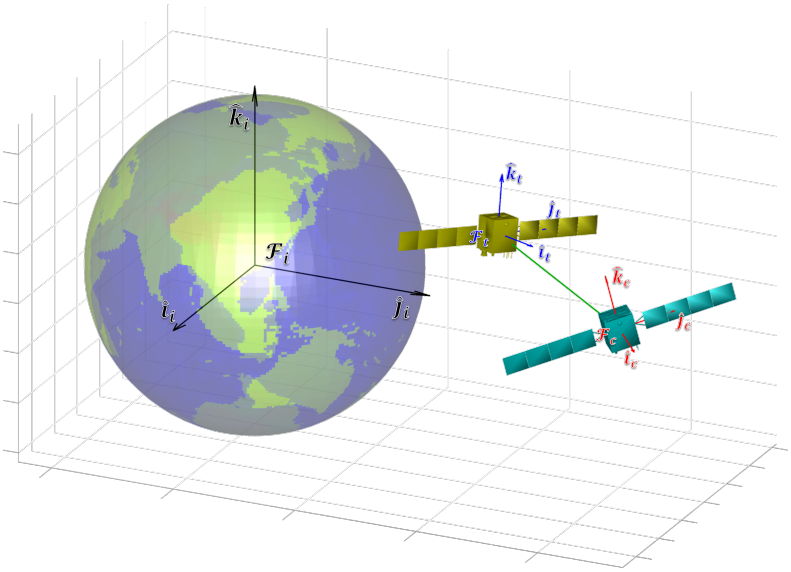

Fig. 1 Definitions of the Earth-Centered Inertial (ECI) frame ($\mathcal{F}_i$), the target body-fixed frame ($\mathcal{F}_t$), and the chaser body-fixed frame ($\mathcal{F}_c$).

The skew-symmetric matrix operator $S(\cdot) : \mathbb{R}^3 \to \mathbb{R}^{3\times3}$ maps a three-dimensional vector $x = [x_1, x_2, x_3]^\top \in \mathbb{R}^3$ into a cross-product matrix defined as:

$$S(x) = \begin{bmatrix} 0 & -x_3 & x_2 \\ x_3 & 0 & -x_1 \\ -x_2 & x_1 & 0 \end{bmatrix}. \tag{7}$$

For any two vectors $x, y \in \mathbb{R}^3$, the operator $S(\cdot)$ satisfies the standard cross-product relationship $S(x)y = x \times y = -S(y)x$.

To accurately describe the orbital and relative motions of the spacecraft, this study utilizes three reference frames as shown in Fig. 1. The first is the Earth-Centered Inertial (ECI) frame $\mathcal{F}_i$, whose origin is located at the center of mass of the Earth. Within this frame, the unit vector $\hat{i}_i$ points toward the direction of the vernal equinox, $\hat{k}_i$ points toward the North Pole, and $\hat{j}_i$ completes the right-handed orthogonal triad. In addition to the inertial frame, two local coordinate systems are employed: the chaser body-fixed frame $\mathcal{F}_c \triangleq \{O_c, \hat{i}_c, \hat{j}_c, \hat{k}_c\}$ and the target body-fixed frame $\mathcal{F}_t \triangleq \{O_t, \hat{i}_t, \hat{j}_t, \hat{k}_t\}$. The origins O_c and O_t are located at the center of mass of the chaser and target spacecraft, respectively, with their coordinate axes rigidly fixed to each corresponding body. The relative motion dynamics presented in this work [16, 17] are fundamentally established and expressed with respect to the chaser body-fixed frame $\mathcal{F}_c$.

3.1 Relative Attitude Kinematics and Dynamics

Before detailing the governing equations for relative attitude, we first define the key angular velocity vectors. Let $\omega_{i,c}^c$ and $\omega_{i,t}^t$ denote the angular velocities of the chaser frame $\mathcal{F}_c$ and the target frame $\mathcal{F}_t$ relative to the inertial frame $\mathcal{F}_i$, expressed in their respective body-fixed coordinates. The relative attitude of the chaser with respect to the target is parameterized using the Modified Rodrigues Parameters (MRP), denoted by $\sigma = [\sigma_x, \sigma_y, \sigma_z]^\top \in \mathbb{R}^3$. Based on this representation, the rotation matrix $R_t^c \in \mathrm{SO}(3)$, which transforms vectors from the target frame $\mathcal{F}_t$ to the chaser frame $\mathcal{F}_c$, is formulated as follows:

$$R_t^c = I_3 - \frac{4(1-\sigma^\top\sigma)}{(1+\sigma^\top\sigma)^2} S(\sigma) + \frac{8S(\sigma)^2}{(1+\sigma^\top\sigma)^2}. \tag{8}$$

The kinematic equation governing the MRP is given by:

$$\dot{\sigma} = \frac{1}{4}\left[(1-\sigma^\top\sigma)I_3 + 2S(\sigma) + 2\sigma\sigma^\top\right]\omega, \tag{9}$$

where I_3 denotes the 3×3 identity matrix, and $\omega \in \mathbb{R}^3$ represents the relative angular velocity between the two satellites, expressed in the chaser frame. This relative angular velocity is defined as

$$\omega = \omega_{i,c}^c - R_t^c \omega_{i,t}^t. \tag{10}$$

The equation of motion for the relative angular velocity ω is derived from Euler's rotational equations. Let $J_c \in \mathbb{R}^{3\times3}$ denote the symmetric positive-definite inertia matrix of the chaser spacecraft, and $M \in \mathbb{R}^3$ represent the control torque applied to the chaser, expressed in its body-fixed frame $\mathcal{F}_c$. By algebraically consolidating the Coriolis and gyroscopic coupling terms, the relative attitude dynamics can be expressed as a single comprehensive equation [14]:

$$\dot{\omega} = J_c^{-1}\left(C(\omega)\omega + D(\omega) + M\right), \tag{11}$$

where:

$$\begin{aligned} C(\omega) &= -J_c S(R_t^c\omega_{i,t}^t) - S(R_t^c\omega_{i,t}^t)J_c + S(J_c(\omega + R_t^c\omega_{i,t}^t)) \\ D(\omega) &= -S(R_t^c\omega_{i,t}^t)J_c R_t^c\omega_{i,t}^t - J_c R_t^c\dot{\omega}_{i,t}^t. \end{aligned} \tag{12}$$

3.2 Relative Translational Kinematics and Dynamics

Following the definition of the relative attitude, we now establish the equations governing the relative translational motion. The relative position vector $\rho \in \mathbb{R}^3$ of the chaser spacecraft with respect to the

target, expressed in the chaser body-fixed frame $\mathcal{F}_c$, is defined as

$$\rho = r_c - R_t^c r_t, \tag{13}$$

where $r_c \in \mathbb{R}^3$ and $r_t \in \mathbb{R}^3$ denote the inertial position vectors of the chaser and target spacecraft, respectively. The relative translational kinematics is governed by the following differential equation:

$$\dot{\rho} = v - S(\omega_{i,c}^c)\rho, \tag{14}$$

where $v \in \mathbb{R}^3$ represents the relative velocity between the two spacecraft, expressed in $\mathcal{F}_c$. According to the fundamental equations of the two-body problem, the relative translational dynamics can be formulated as

$$\dot{v} = -S(\omega_{i,c}^c)v - \frac{\mu}{\|r_c\|^3} r_c - R_t^c \dot{v}_t + \frac{F}{m_c}, \tag{15}$$

where m_c is the mass of the chaser spacecraft, and $F \in \mathbb{R}^3$ is the control force applied to the chaser in $\mathcal{F}_c$. In this formulation, the term $-S(\omega_{i,c})v$ accounts for the Coriolis effect. The term $-\mu r_c/\|r_c\|^3$ represents the gravitational acceleration acting on the chaser, where $\mu = 3.986004 \times 10^{14}\ \mathrm{m}^3/\mathrm{s}^2$ is the standard gravitational parameter of the Earth. Lastly, $\dot{v}_t$ denotes the inertial acceleration of the target spacecraft.

4 Cascaded Control Barrier Function

Consider a class of cascaded nonlinear control-affine systems represented by:

$$\begin{aligned} \dot{x}_1 &= f_1(x_1) + g_1(x_1)x_2 \\ \dot{x}_2 &= f_2(x_2) + g_2(x_2)x_3 \\ &\vdots \\ \dot{x}_n &= f_n(x_n) + g_n(x_n)u. \end{aligned} \tag{16}$$

$x_i \in \mathbb{R}^{d_i}$ for $i \in \{1, \ldots, n\}$ denotes the state vector at the i-th hierarchical layer, and $u \in \mathbb{R}^m$ is the actual control input applied to the final dynamic layer. In this strict-feedback form, the state of the subsequent layer x_{i+1} acts as the virtual control input for the preceding layer x_i.

To enforce safety across the entire system, the CCBF applies a sequential safety filter at each individual cascade layer. Let r_i^{nom} denote the nominal virtual control command generated by a baseline controller. At the first layer, the primary safety requirement is encoded by a continuously differentiable barrier function $\psi_1(x_1) \geq 0$. The safe virtual control input r_2^*, which dictates the desired safe behavior for x_2, is obtained by solving a layer specific QP:

$$\begin{aligned} r_2^* = \underset{r_2 \in \mathcal{R}_2}{\operatorname{argmin}} \quad & \frac{1}{2}\|r_2 - r_2^{\mathrm{nom}}\|^2 \\ \text{s.t.} \quad & L_{f_1}\psi_1(x_1) + L_{g_1}\psi_1(x_1)r_2 + \alpha_1(\psi_1(x_1)) \geq 0. \end{aligned} \tag{17}$$

As the cascade descends, the safe virtual input r_{i+1}^* generated by the upper layer must be tracked by the current layer's state x_i, while simultaneously satisfying the system's safety bounds. Analogous to the principle of HOCBF [13], the CCBF for the i-th layer is recursively defined. Let $\bar{x}_i = [x_1^\top, \ldots, x_i^\top]^\top$ denote the augmented state up to layer i, and $\psi_1(x_1) = h(x_1)$. The sequence of barrier functions is formulated as:

$$\psi_{i+1}(\bar{x}_{i+1}) = \frac{\partial \psi_i}{\partial \bar{x}_i}\dot{\bar{x}}_i + \alpha_i(\psi_i(\bar{x}_i)), \quad i \in \{1, \ldots, n\}. \tag{18}$$

By sequentially differentiating the barrier function $\psi_i(\bar{x}_i)$, the generic safety constraint for the i-th intermediate layer is yielded. The corresponding virtual control input r_{i+1}^* is solved via:

$$\begin{aligned} r_{i+1}^* = \underset{r_{i+1}\in\mathcal{R}_{i+1}}{\operatorname{argmin}} \quad & \frac{1}{2}\|r_{i+1} - r_{i+1}^{\text{nom}}\|^2 \\ \text{s.t.} \quad & \frac{\partial \psi_i}{\partial \bar{x}_i} g_i(\bar{x}_i) r_{i+1} + \Gamma_i(\bar{x}_i) + \alpha_i(\psi_i(\bar{x}_i)) \geq 0, \end{aligned} \tag{19}$$

where $\Gamma_i(\bar{x}_i)$ encapsulates all remaining state-dependent derivative terms independent of r_{i+1}. This sequential filtering cascade continues down to the n-th layer, where the actual control input u is finally optimized to ensure the forward invariance of the interconnected system.

Remark 1 (*Safety Consistency in Cascaded Architectures*): Standard HOCBF formulations enforce high-order derivative constraints within a single monolithic QP at the final dynamic control level. This reactive structure often restricts the feasible control space and induces boundary-riding behaviors when the nominal control objective conflicts with the safety boundary. In contrast, the proposed CCBF establishes *safety consistency* by integrating with the backstepping architecture. By employing a cascaded multi-QP framework, the CCBF sequentially ensures the safety of the virtual control references at each intermediate layer before determining the final dynamic input. This layer-by-layer enforcement structurally decouples the safety conditions, directly facilitating the tuning tractability addressed in the subsequent remark.

Remark 2 (*Tuning Tractability and Constraint Decomposition*): The proposed layer-by-layer decomposition provides significant practical advantages in control design. In standard monolithic HOCBFs, when the QP solver encounters an infeasible state, identifying which specific extended class $\mathcal{K}$ function α_i requires adjustment is practically intractable due to the coupled nature of the high-order derivatives. The CCBF isolates the optimization process at each step. Although this approach maintains the mathematical order of the partial derivatives, the stepwise isolation provides clear traceability. If a specific cascaded layer approaches infeasibility, the corresponding α parameter can be adjusted independently, facilitating a less conservative and more tunable control design.

4.1 Controller and Safety Filter for Spacecraft Rendezvous

In this study, a backstepping-based Control Lyapunov Function evaluated via Quadratic Programming (CLF-QP) is employed as the nominal controller for the spacecraft rendezvous maneuver. For the translational motion, the primary objective is to converge to a desired relative position $\rho_r = [1, 0, 0]^\top$ expressed in the target frame $\mathcal{F}_t$. Accordingly, the Lyapunov function for the first kinematic layer is defined as:

$$V_1^t(x) = \frac{1}{2}\left(\rho_t - \rho_r\right)^\top \left(\rho_t - \rho_r\right), \tag{20}$$

where $\rho_t = R_c^t \rho$. To track the virtual velocity control input v_r generated by the first layer, the Lyapunov function for the second dynamic layer is constructed as:

$$V_2^t(x) = V_1^t(x) + \frac{1}{2}\left(v - v_r\right)^\top \left(v - v_r\right). \tag{21}$$

Similarly, to control the attitude of the chaser spacecraft, the Lyapunov functions for the first kinematic layer and the final dynamic layer are defined using the MRP vector σ and angular velocity ω:

$$\begin{aligned} V_1^a(x) &= \frac{1}{2}\sigma^\top \sigma, \\ V_2^a(x) &= V_1^a(x) + \frac{1}{2}\left(\omega - \omega_r\right)^\top \left(\omega - \omega_r\right). \end{aligned} \tag{22}$$

Based on these sequential Lyapunov functions, the nominal control inputs are synthesized by solving the following CLF-QP optimization problem at each respective layer:

$$\begin{aligned} \min_{u,\delta} \quad & \frac{1}{2}u^\top H u + p\delta^2 \\ \text{s.t.} \quad & L_f V(x) + L_g V(x) u + \gamma(V(x)) \leq \delta, \\ & u_{\text{lb}} \leq u \leq u_{\text{ub}}. \end{aligned} \tag{23}$$

Here, the decay rates for the CLF constraints at each backstepping layer are set to $\gamma_\rho = 0.8$, $\gamma_v = 0.08$, $\gamma_\sigma = 3$, and $\gamma_\omega = 0.1$. The parameter p is a large penalty weight for the slack variable δ to ensure the strict feasibility of the QP, and H is a positive definite weight matrix. Within this cascaded architecture, the generalized control variable u denotes the virtual reference commands (v_r and ω_r) when evaluated at the kinematic layers, and the actual physical control efforts (force F and moment M) at the subsequent dynamic layers.

While the attitude tracking is entirely governed by the unconstrained CLF-QP formulation, the translational motion must adhere to complex spatial boundaries during the proximity operation. To enforce this, a semi-cubical parabola-based path constraint is adopted from [14]. The line-of-sight relative position expressed in the target body frame is denoted as $\rho_t = (R_t^c)^\top \rho = R_c^t \rho \equiv [x_t, y_t, z_t]^\top$. Based on this coordinate system, the geometric barrier function $h(x)$, which is visually represented in Fig. 2, restricts the chaser's trajectory as follows:

$$h(x) = \alpha_h (x_t - \delta_h)^3 - y_t^2 - z_t^2. \tag{24}$$

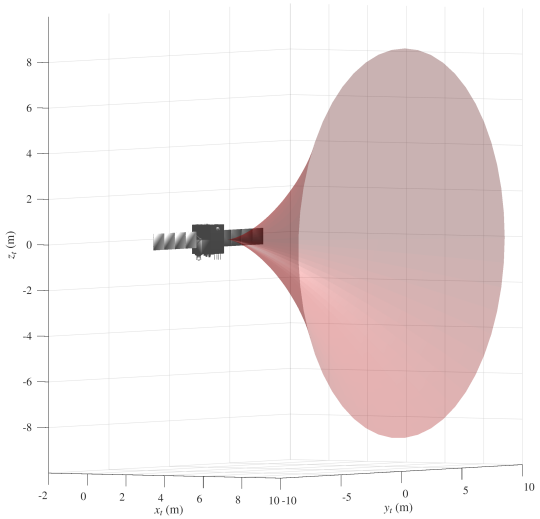

Fig. 2 Three-dimensional visualization of the semi cubical cone path constraint corridor defined by parameters α_h and δ_h.

To guarantee safety within the proposed cascaded architecture, this geometric boundary is mapped to the CCBF formulation defined in Eq. (19). For the first kinematic layer, the foundational barrier state is defined as $\psi_1(x) = h(x)$. To ensure safety while adhering to the principle of minimal intervention, the virtual velocity reference v_r^* is obtained by filtering the nominal command v_r^{nom} (derived from the translational CLF-QP) through the following CBF-QP formulation:

$$\begin{aligned} v_r^* = \underset{v_r \in \mathcal{V}}{\text{argmin}} \quad & \frac{1}{2}\|v_r - v_r^{\text{nom}}\|^2 \\ \text{s.t.} \quad & L_f \psi_1(x) + L_g \psi_1(x) v_r + \alpha_1(\psi_1(x)) \geq 0. \end{aligned} \tag{25}$$

For the second dynamic layer where the actual control force F is synthesized, the extended barrier function is defined as $\psi_2(x) = \dot{\psi}_1(x) + \alpha_1(\psi_1(x))$. The corresponding safety filter calculates the safe control input F^* by minimally modifying the nominal force F^{nom} via the secondary CBF-QP:

$$\begin{aligned} F^* = \underset{F\in\mathcal{F}}{\operatorname{argmin}} \quad & \frac{1}{2}\|F - F^{\text{nom}}\|^2 \\ \text{s.t.} \quad & L_f\psi_2(x) + L_g\psi_2(x)F + \alpha_2(\psi_2(x)) \geq 0 \\ & F_{\text{lb}} \leq F \leq F_{\text{ub}}. \end{aligned} \tag{26}$$

The complete closed-loop control architecture for the translational motion is illustrated in Fig. 3. The overall system operates within a feedback loop where the controller is structurally decomposed into a two-stage cascaded framework before being applied to the spacecraft plant. Specifically, the first stage addresses the kinematic level. A CLF-QP computes the nominal virtual velocity v_r^{nom}, which is immediately processed by a CBF-QP safety filter to generate a safe virtual reference v_r^*. Subsequently, the second stage addresses the dynamic level. By tracking this safe virtual reference v_r^*, a subsequent CLF-QP computes the nominal control force F^{nom}, followed by a final CBF-QP safety filter that synthesizes the safe physical control input F^* to be applied to the system. The mathematical expansion of the barrier

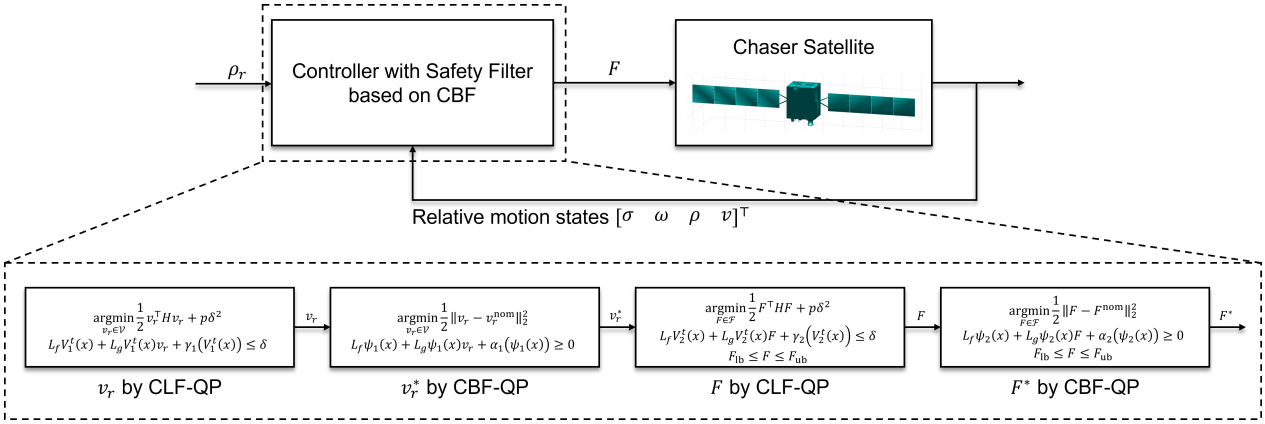

Fig. 3 Block diagram of the proposed cascaded control architecture for translational motion.

functions are detailed in the Appendix.

5 Numerical Simulation

To verify the proposed CCBF framework and compare it with the standard HOCBF, numerical simulations were performed using MATLAB R2025a. The physical properties of the chaser satellite are modeled with a mass of $m_c = 38.2\,\text{kg}$. To reflect hardware limitations, the control inputs are subject to saturation constraints. The control force and torque are bounded by $\pm 20\,\text{N}$ and $\pm 5\,\text{N·m}$ along each axis, respectively. The inertia matrix of the chaser satellite, denoted as J_c ($\text{kg} \cdot \text{m}^2$), is given by:

$$J_c = \begin{bmatrix} 124.4 & 22.5 & -21.5 \\ 22.5 & 163.6 & -7.0 \\ -21.5 & -7.0 & 128.3 \end{bmatrix}. \tag{27}$$

The barrier function employed in these simulations is the semi-cubical cone proposed in [14], which is defined using the relative position vector expressed in the target frame, $\rho_t = R_c^t\rho$. This spatial constraint is mathematically formulated in Eq. (32) and visually illustrated in Fig. 2. The parameter α_h determines the width of the cone; a larger value of α_h results in a wider allowable approach corridor. The parameter

δ_h defines the offset distance from the origin of the target frame $\mathcal{F}_t$, indicating the exact position where the rendezvous docking is completed. For the present simulation scenarios, the cone width parameter is set to $\alpha_h = 0.1$, and the offset is chosen as $\delta_h = 1$. The apex of the semi-cubical cone is located at a distance of 1 m along the $\hat{i}_t$-axis of the target frame. The formulation utilized for the safety filters, which applies to both the CCBF and the baseline HOCBF used for comparative analysis, is detailed in the Appendix from Eq. (33-42). For the CBFs associated with the translational kinematics in Eq. (14) and the relative dynamics in Eq. (15), the extended class $\mathcal{K}$ functions are chosen as linear functions. Their corresponding coefficients are set to $\alpha_\rho = 0.8$ and $\alpha_v = 0.1$, respectively.

To evaluate the performance of the proposed control frameworks, the numerical simulations are initialized with specific orbital and relative state parameters. The target satellite is assumed to be operating in an elliptical orbit, defined by a semi-major axis of $a = 7,702,455$ m, an eccentricity of $e = 0.12$, and an orbital inclination of $i = 30°$. The remaining classical orbital elements, including the right ascension of the ascending node (Ω), the argument of perigee (ω), and the initial true anomaly (f_0), are all set to 0°. It is assumed that the target satellite maintains a fixed attitude with respect to the ECI frame $\mathcal{F}_i$, meaning that both its angular velocity $\omega_{i,t}^t$ and angular acceleration $\dot{\omega}_{i,t}^t$ are zero. For the relative dynamics, the chaser satellite is initially placed at a relative position of $\rho_0 = [47.2, -16.6, 38.4]^\top$ m with an initial relative velocity of $v_0 = [-0.2, -0.3, -0.1]^\top$ m/s with respect to the target frame. Furthermore, the initial rotational kinematics and dynamics are defined by the MRP $\sigma_0 = [-0.1, 0.12, 0.1]^\top$ and the relative angular velocity $\omega_0 = [0.05, -0.03, 0.07]^\top$ rad/s, respectively.

5.1 Scenario 1: Performance Comparison of the Proposed CCBF Framework

This scenario evaluates the cascaded system defined in Eq. (16) under three distinct control strategies during a rendezvous and docking maneuver: the nominal CLF-QP controller, the standard HOCBF, and the proposed CCBF framework. Both the HOCBF and the proposed CCBF utilize the identical barrier candidate given in Eq. (32). Figure 4 illustrates the resulting three-dimensional spatial trajectories of the chaser satellite, which are represented with respect to the target reference frame, denoted as $\mathcal{F}_t$. As illustrated by the nominal CLF-QP responses in Fig. 4 and Fig. 6a, the controller exhibits a significant overshoot in the relative position during the approach phase. Such transient behavior implies that the chaser satellite is exposed to a collision risk with the target satellite during close-proximity operations. These results emphasize the necessity of executing rendezvous and docking maneuvers while adhering to predefined path constraints to guarantee system safety [14].

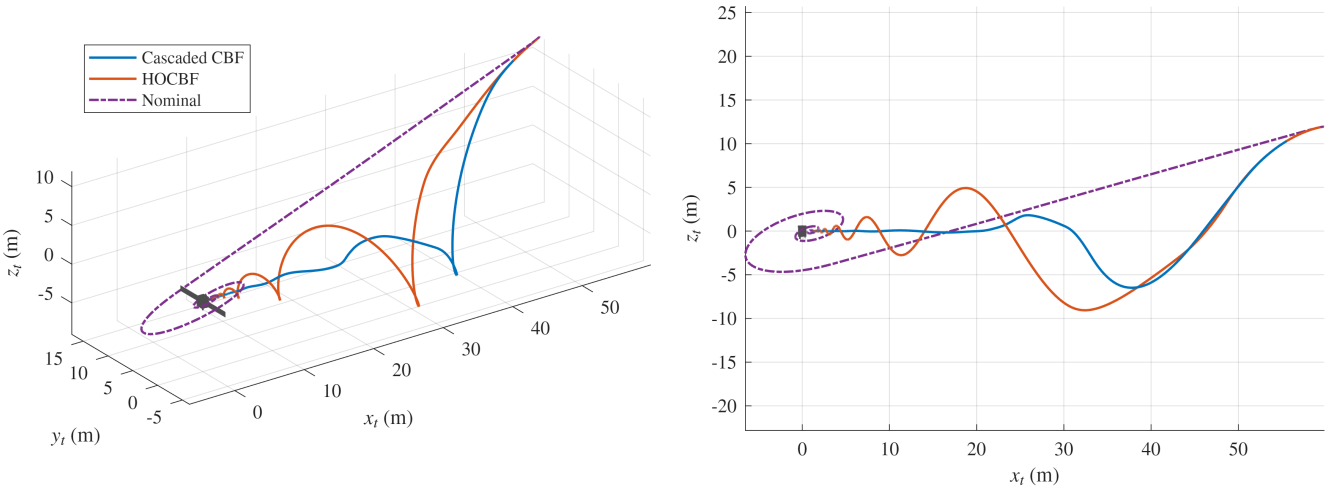

Fig. 4 Three-dimensional relative trajectories of the chaser satellite under the nominal CLF-QP, HOCBF, and the proposed CCBF frameworks.

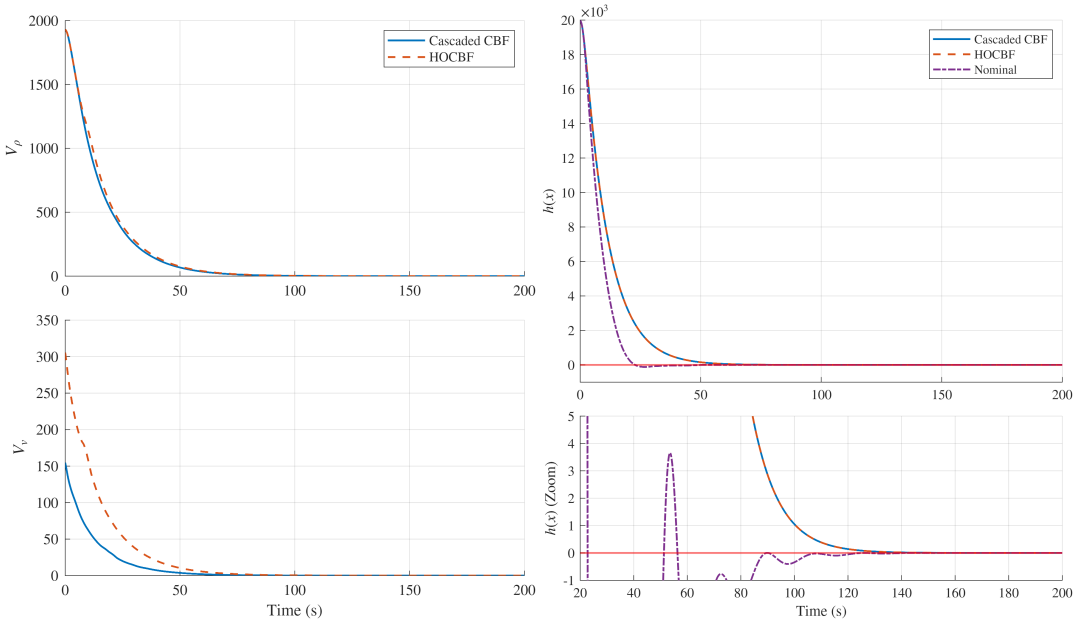

(a) Lyapunov function (V) **(b) Control barrier function (h)**

Fig. 5 Responses of the stability and safety certification functions. (a) Lyapunov function values demonstrating convergence and (b) control barrier function values ensuring safety.

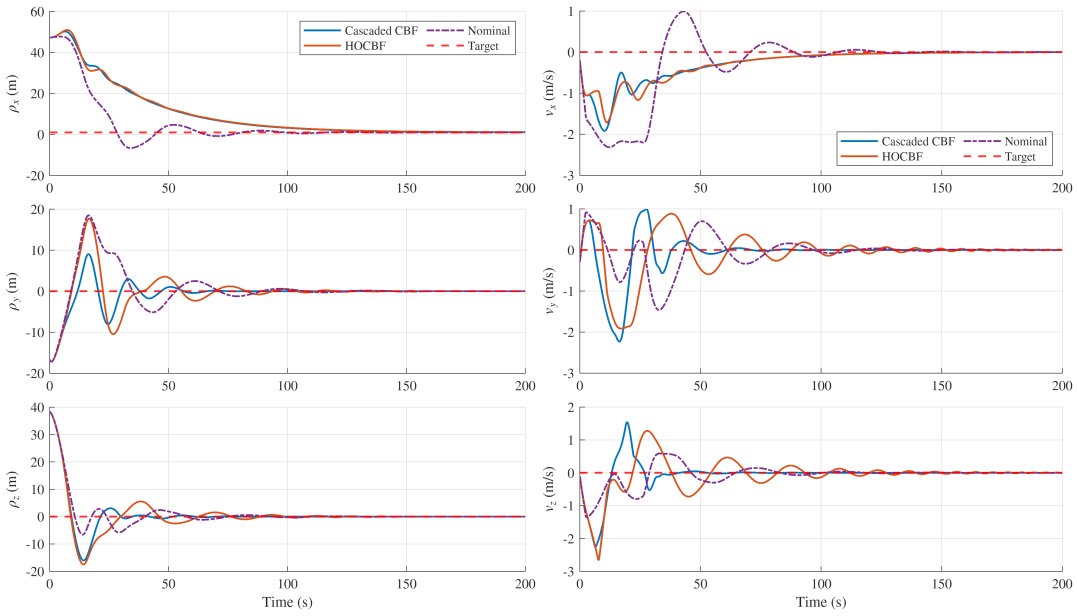

(a) Relative position (ρ) **(b) Relative velocity (v)**

Fig. 6 Responses of the translational relative motion for the chaser satellite. (a) Relative position and (b) relative velocity profiles under the nominal CLF-QP, HOCBF, and the proposed CCBF.

The integration of barrier functions successfully mitigates this collision risk. As demonstrated in Fig. 5b, both the HOCBF and the proposed CCBF maintain the required safety margins ($h(x) \geq 0$) throughout the entire maneuver, safely confining the chaser satellite within the designated safe corridor.

Although both barrier-based frameworks guarantee safety, their convergence behaviors differ due to the geometric stringency of the path constraints. The semi-cubical cone employed in this rendezvous and docking scenario imposes a non-linear spatial envelope, where the allowable lateral deviations in the y_t and z_t directions become progressively restricted as the chaser approaches the destination target.

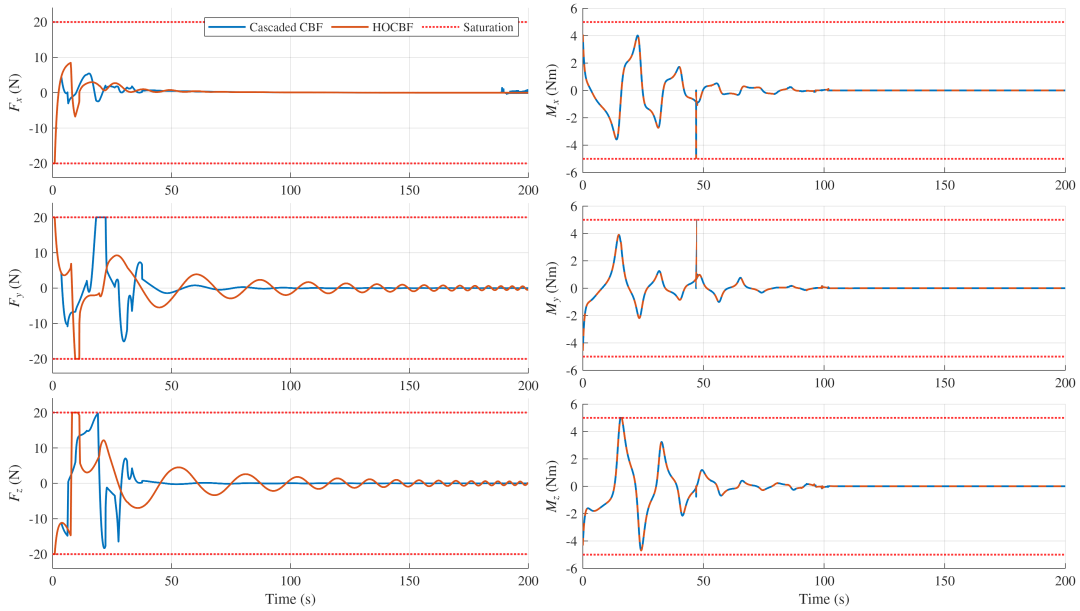

(a) Control force (F) **(b) Control moment (M)**

Fig. 7 Responses of the control inputs for the chaser satellite. (a) Control force and (b) control moment profiles under the HOCBF and the proposed CCBF.

The standard HOCBF operates as a CBF-QP based safety filter at the control input level u. Because it is formulated based on the principle of minimal intervention, when the nominal controller pushes the system toward the safety limit, the resulting state trajectory tends to slide along the safety boundary.

In contrast, the proposed CCBF framework ensures the safety of the virtual control reference, thereby establishing safety consistency throughout the cascaded dynamics. By addressing safety at the kinematic level, the CCBF prevents the boundary-riding response. In the context of this rendezvous and docking scenario, the geometric nature of the semi-cubical cone dictates that the safe gradient at the kinematic level progressively aligns with the target direction as the chaser approaches the destination. Because the CCBF framework ensures safety at this stage, the resulting virtual control reference yields a trajectory vector oriented directly toward the target state. This alignment illustrates the practical advantage of maintaining safety consistency. As depicted in the Lyapunov function responses in Fig. 5a and the translational kinematics in Fig. 6, this structural safety enables the CCBF to achieve a more direct convergence to the target relative position and velocity. Consequently, it leads to a steady reduction of the tracking errors without oscillations.

Regarding the control inputs shown in Fig. 7, the control moments M generated by the HOCBF and the CCBF are identical, which is theoretically consistent as the barrier constraints affect the translational kinematics. However, a quantitative analysis of the control force F reveals a clear practical trade-off between the control effort and the resulting maneuver efficiency. Evaluating the total control effort using the L_2 norm ($\int_0^T \|F\|_2^2 dt$) yields 8176.71 $\mathrm{N}^2\cdot\mathrm{s}$ for the HOCBF and 9016.69 $\mathrm{N}^2\cdot\mathrm{s}$ for the proposed CCBF. By proactively utilizing this additional control effort to align the trajectory away from the boundary early on, the CCBF framework streamlines the maneuver and yields a total path length of 104.84 m for the standard HOCBF down to 80.59 m. This 23.13% reduction in spatial travel distance demonstrates that the kinematic-level safety enforcement effectively eliminates boundary-riding and unnecessary detours, making the slight increase in control effort a highly worthwhile trade-off for a safer and more direct rendezvous.

5.2 Scenario 2: Monte-Carlo Simulation

To verify the safety consistency and control efficiency of the proposed CCBF framework against the standard HOCBF, 100 independent runs of Monte-Carlo simulation were conducted. The tuning parameters, including the decay rates γ for the CLF-QP and the extended class $\mathcal{K}$ functions $\alpha(\cdot)$ within the safety filters, were maintained identical to those established in Scenario 1.

A set of 100 distinct initial conditions was randomly generated subject to specific bounds. The initial relative attitude, parameterized by the MRP σ, was uniformly sampled within the interval of -0.0873 to 0.0873 for each axis. Similarly, the initial relative angular velocity ω was uniformly distributed between -3°/s and 3°/s per axis. The initial relative distance between the chaser and the target satellite was fixed at 50 m. The specific initial position vectors were randomly generated to satisfy the predefined semi-cubical cone safety constraint $h(x) \geq 0$, from Eq. (24). Finally, the initial relative velocity was uniformly sampled from -0.1 m/s to 0.1 m/s along each axis defined in the chaser body-fixed frame $\mathcal{F}_c$.

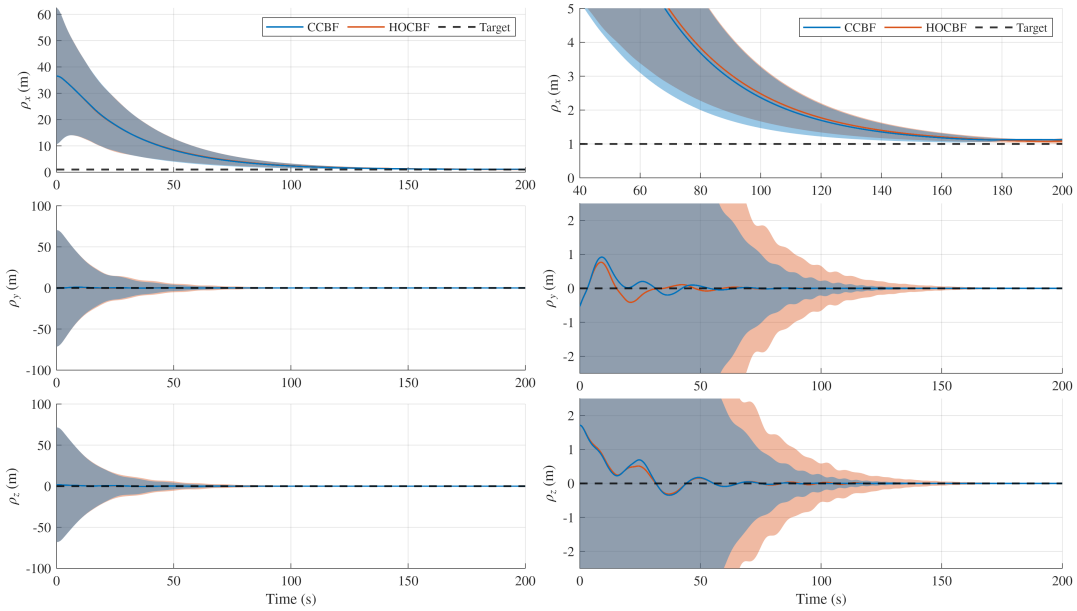

(a) Relative position (ρ) **(b) Relative position (ρ) (Zoomed)**

Fig. 8 Statistical responses of the relative position trajectories from Monte-Carlo simulation. The solid lines denote the mean trajectories, and the envelopes represent the 3-std bounds.

In Fig. 8, the statistical responses of the relative position trajectories are evaluated across Monte-Carlo simulations. The right subfigure provides a zoomed-in view to clearly present the transient behaviors during the approach phase. In these plots, the solid lines indicate the mean trajectory computed from the simulation data, while the semi-transparent envelopes surrounding the mean values illustrate the 3-std (standard deviation) confidence bounds. From the envelopes presented in Fig. 8b, it is evident that the lateral relative positions, ρ_y and ρ_z, converge faster under the CCBF framework compared to the HOCBF. In terms of safety consistency, this result implies that the boundary-riding behavior induced by the standard HOCBF delays the rendezvous convergence. Furthermore, the mean trajectory of the longitudinal position ρ_x demonstrates a marginally faster convergence rate under the proposed CCBF.

Fig. 9 presents the responses of the Lyapunov and barrier functions evaluated across the 100 Monte-Carlo simulation runs. Unlike the confidence bounds shown in Fig. 8, the semi-transparent envelopes in these subfigures indicate the minimum and maximum values derived from all simulation data, while the solid lines represent the mean responses. As depicted in Fig. 9a, both the HOCBF and the proposed CCBF frameworks successfully ensure asymptotic stability, as the Lyapunov functions V_ρ and V_v converge to zero regardless of the randomized initial conditions. The mean trajectory of V_v reveals that the CCBF achieves faster convergence compared to the HOCBF. For V_ρ, although the mean trajectories of both

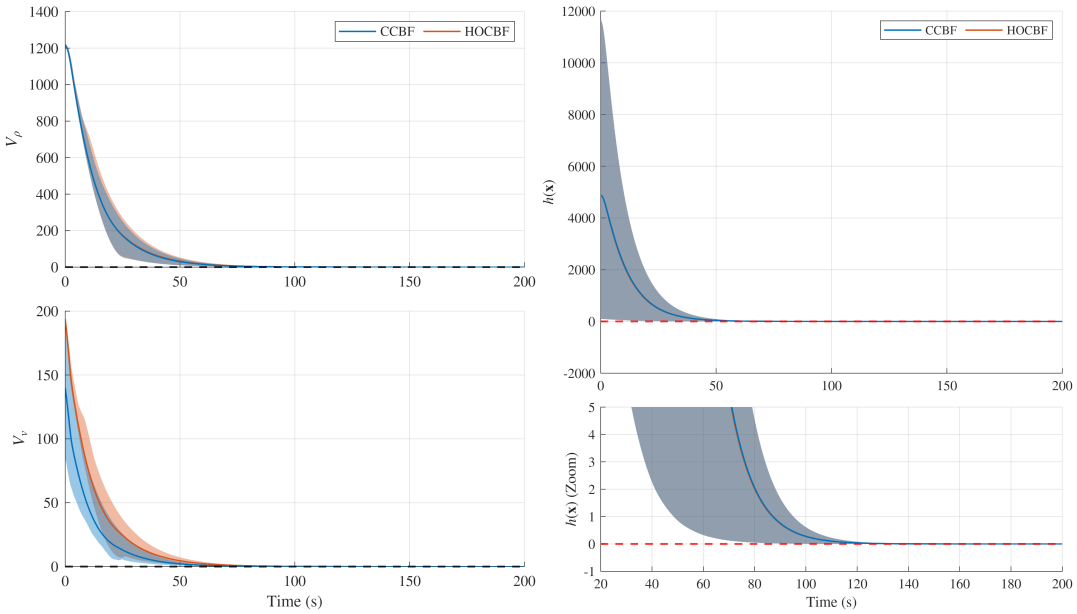

(a) Lyapunov functions (V_ρ, V_v) **(b) Barrier function ($h(\mathbf{x})$)**

Fig. 9 Lyapunov and barrier functions responses from the Monte-Carlo simulation. The solid lines denote the mean trajectories, while the envelopes represent the minimum and maximum bounds across all simulations.

frameworks are nearly identical, the envelope of the CCBF is bounded within that of the HOCBF. This indicates that the proposed CCBF yields a more consistent and robust response against variations in initial conditions. Fig. 9b demonstrates the rigorous enforcement of the safety constraints. The lower bounds of the barrier function envelopes for both controllers never violate the safety, $h(\mathbf{x}) \geq 0$, throughout the entire maneuver, numerically proving the forward invariance of the safe set.

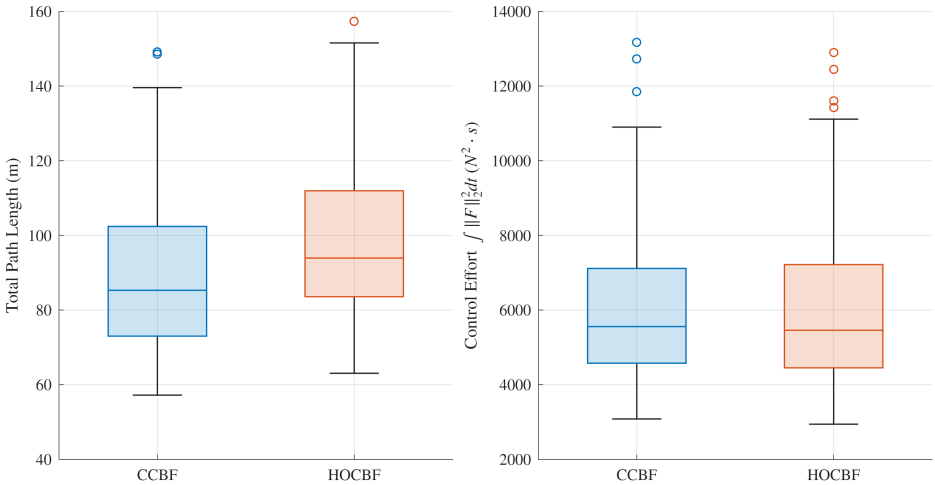

Fig. 10 Statistical distributions of the total traveled path length and control effort. The box plots illustrate the median, interquartile range, and variance for each framework.

To quantitatively assess the maneuver efficiency and robustness, Fig. 10 illustrates the statistical distributions of the total traveled path length and the required control effort. Regarding the spatial trajectory, the proposed CCBF achieves a lower median path length of 85.29 m compared to 93.92 m for the standard HOCBF. An analysis of the upper whiskers reveals that the HOCBF extends up to 151.5 m in adverse scenarios, whereas the CCBF effectively suppresses the worst-case trajectory expansion to 139.6 m. This demonstrates that the kinematic-level safety enforcement prevents the detours. Conversely, the evaluation of the control effort presents a slight increase in the median value for the CCBF 5557 $N^2 \cdot s$

compared to the HOCBF 5457 $N^2 \cdot s$. However, observing the dispersion of the data demonstrates the structural advantage of the proposed framework. The CCBF yields a tighter interquartile range (4576 to 7114 $N^2 \cdot s$) and narrower whisker bounds (3082 to 10899 $N^2 \cdot s$) than those of the HOCBF, (4451 to 7217 $N^2 \cdot s$, and 2942 to 11112 $N^2 \cdot s$, respectively).

6 Conclusion

In this paper, a Cascaded Control Barrier Function (CCBF) framework was proposed to ensure the safety of spacecraft rendezvous and docking maneuvers under spatial path constraints. By integrating barrier conditions within a cascaded backstepping architecture, the proposed framework establishes safety consistency starting from the kinematic level. As demonstrated in the simulation, this proposed CCBF framework prevents the reactive boundary-riding behaviors typically observed in standard High-Order CBFs. Consequently, this structurally embedded safety consistency naturally aligns the system trajectory with the highly restrictive semi-cubical cone path constraints, while the layer-by-layer constraint decomposition provides clear traceability and significant practical benefits in parameter tuning.

Appendix

This appendix provides the mathematical derivations required to implement the proposed cascaded control barrier function framework in simulation. To successfully apply this cascaded safety architecture, the barrier function constraints must be explicitly formulated with respect to the virtual control input v (relative velocity represented in $\mathcal{F}_c$) at the kinematic level, and synthesized with respect to the actual control force F at the dynamic level. Before presenting the detailed expansion of these dynamic constraints, this section introduces essential mathematical lemmas and establishes the rotational kinematic relations that serve as the prerequisite basis for the subsequent proofs.

Lemma 1. *For any vectors $a, b \in \mathbb{R}^3$, the double cross-product yields the following skew-symmetric matrix identity:*

$$S(a \times b) = S(S(a)b) = S(a)S(b) - S(b)S(a). \tag{28}$$

Lemma 2. *For a rotation matrix $\mathcal{R} \in \mathrm{SO}(3)$ and any vectors $a, b \in \mathbb{R}^3$, the cross-product is preserved under rotation:*

$$\mathcal{R}(S(a)b) = S(\mathcal{R}a)\mathcal{R}b \implies \mathcal{R}S(a) = S(\mathcal{R}a)\mathcal{R}. \tag{29}$$

Lemma 3. *$R_t^c \in \mathrm{SO}(3)$ denotes the rotation matrix from the target body frame to the chaser body frame. The time derivative of this rotation matrix is given by:*

$$\frac{d}{dt}R_t^c = -S(\omega)R_t^c, \tag{30}$$

where ω is the relative angular velocity. To analyze the relative position vector expressed in the target body frame, denoted as $\rho_t = (R_t^c)^\top \rho = R_c^t \rho \equiv [x_t, y_t, z_t]^\top$, it is necessary to derive the time derivative of the transposed rotation matrix R_c^t. Utilizing the property of skew-symmetric matrices where $S(\omega)^\top = -S(\omega)$, the time derivative is derived as follows:

$$\begin{aligned} \frac{d}{dt}R_c^t &= \frac{d}{dt}(R_t^c)^\top \\ &= \left(-S(\omega)R_t^c\right)^\top \\ &= R_c^t S(\omega). \end{aligned} \tag{31}$$

Control Barrier Function Formulation

To ensure the safety of the spacecraft during proximity operations, spatial constraints must be enforced. A differentiable constraint is formulated using a CBF, where a semi-cubical parabola-based curve is selected [14] to restrict the chaser's approach trajectory. The barrier function $h(x)$ is defined with respect to the target frame coordinates:

$$h(x) = \alpha_h(x_t - \delta_h)^3 - y_t^2 - z_t^2, \tag{32}$$

where $\alpha_h > 0$ dictates the strictness of the spatial boundary, and δ_h represents the desired safe standoff distance along the $\hat{i}_t$-axis. To enforce the forward invariance of the safe set, the time derivative of the barrier function is evaluated using the chain rule:

$$\dot{h}(x) = \left(\frac{\partial h(x)}{\partial \rho_t}\right)^\top \dot{\rho}_t. \tag{33}$$

The partial derivative of the barrier function with respect to ρ_t is computed as:

$$\frac{\partial h(x)}{\partial \rho_t} = \begin{bmatrix} 3\alpha_h(x_t - \delta_h)^2 & -2y_t & -2z_t \end{bmatrix}^\top. \tag{34}$$

Subsequently, the time derivative of the relative position vector in the target frame, $\dot{\rho}_t$, is evaluated. By substituting (30) alongside the relative translational kinematics Eq. (13), the expression expands to:

$$\begin{aligned} \dot{\rho}_t &= \dot{R}_c^t \rho + R_c^t \dot{\rho} \\ &= R_c^t \left(v + \left(S(\omega) - S(\omega_{i,c}^c) \right) \rho \right). \end{aligned} \tag{35}$$

Leveraging the linearity of the skew-symmetric operator and the fundamental relative motion kinematics (10), it can be shown that $S(\omega) - S(\omega_{i,c}^c) = -S(R_t^c \omega_{i,t}^t)$. Substituting this property back into (35) yields:

$$\dot{\rho}_t = R_c^t \left(v - S(R_t^c \omega_{i,t}^t)\rho \right). \tag{36}$$

Enforcing safety solely at the kinematic level does not guarantee the forward invariance of the actual dynamic system. To impose constraints directly on the control force F, a HOCBF expansion [13] is required for this relative degree two system. The sequence of barrier functions is formulated as:

$$\begin{aligned} h_2(x) &= \dot{h}(x) + \alpha_1 \left(h(x) \right) \geq 0, \\ \dot{h}_2(x) &= \ddot{h}(x) + \alpha_1 \dot{h}(x) + \alpha_2 \left(\dot{h}(x) + \alpha_1 h(x) \right) \geq 0. \end{aligned} \tag{37}$$

To evaluate $\ddot{h}(x)$, the second-order expansion is derived as:

$$\ddot{h}(x) = \dot{\rho}_t^\top \frac{\partial^2 h(x)}{\partial \rho_t^2} \dot{\rho}_t + \left(\frac{\partial h(x)}{\partial \rho_t} \right)^\top \ddot{\rho}_t, \tag{38}$$

where the Hessian matrix $\frac{\partial^2 h(x)}{\partial \rho_t^2}$ is defined as:

$$\frac{\partial^2 h(x)}{\partial \rho_t^2} = \text{diag}\left(6\alpha_h(x_t - \delta_h), -2, -2 \right), \tag{39}$$

where $\text{diag}(\cdot)$ denotes a square diagonal matrix with the specified elements aligned on its main diagonal.

To expand $\ddot{\rho}_t$ and isolate the control force F, we first introduce two essential lemmas regarding skew-symmetric matrices. By differentiating Eq. (36) and substituting the relative translational dynamics Eq. (15), we obtain:

$$\begin{aligned}\ddot{\rho}_t &= \frac{d}{dt}\left(R_c^t\left(v - S(R_t^c\omega_{i,t}^t)\rho\right)\right) \\ &= R_c^t S(\omega)v - R_c^t S(\omega)S(R_t^c\omega_{i,t}^t)\rho - R_c^t S(\omega_{i,c}^c)v - R_c^t S(-S(\omega)R_t^c\omega_{i,t}^t)\rho - R_c^t S(R_t^c\dot{\omega}_{i,t}^t)\rho \cdots \\ &- R_c^t S(R_t^c\omega_{i,t}^t)\dot{\rho} + R_c^t\left(-\frac{\mu}{\|r_c\|^3}r_c - R_t^c\dot{v}_t + \frac{F}{m_c}\right)\end{aligned} \tag{40}$$

To simplify the expanded expression of Eq. (40), we apply the skew-symmetric identity from **Lemma 1** to the nested cross-product term, yielding the following relation:

$$-R_c^t S(-S(\omega)R_t^c\omega_{i,t}^t)\rho = -R_c^t S(R_t^c\omega_{i,t}^t)S(\omega)\rho + R_c^t S(\omega)S(R_t^c\omega_{i,t}^t)\rho. \tag{41}$$

Substituting Eq. (40) back into the original expansion results in the exact cancellation:

$$\ddot{\rho}_t = -R_c^t S(R_t^c\omega_{i,t}^t)\left(v + S(\omega)\rho + \dot{\rho}\right) - S(\dot{\omega}_{i,t}^t)R_c^t\rho + R_c^t\left(-\frac{\mu}{\|r_c\|^3}r_c - R_t^c\dot{v}_t + \frac{F}{m_c}\right). \tag{42}$$

To finalize the formulation, we aim to simplify the first term of (42). According to **Lemma 2** (29), the outer multiplier $-R_c^t S(R_t^c\omega_{i,t}^t)$ can be equivalently expressed as $-S(\omega_{i,t}^t)R_c^t$. Concurrently, the inner component of the first term, $(v + S(\omega)\rho + \dot{\rho})$, can be expanded by substituting the relative translational kinematics from Eq. (14). Recognizing that $S(\omega) - S(\omega_{i,c}^c) = -S(R_t^c\omega_{i,t}^t)$, the inner term is algebraically manipulated to extract the exact form of $\dot{\rho}_t$:

$$v + S(\omega)\rho + \dot{\rho} = 2\left(v - S(R_t^c\omega_{i,t}^t)\rho\right) + S(R_t^c\omega_{i,t}^t)\rho. \tag{43}$$

By pre-multiplying this expanded inner term by $-S(\omega_{i,t}^t)R_c^t$, the entire first term of (42) reduces to:

$$-S\left(\omega_{i,t}^t\right)R_c^t\left[2\left(v - S(R_t^c\omega_{i,t}^t)\rho\right) + S(R_t^c\omega_{i,t}^t)\rho\right] = -2S(\omega_{i,t}^t)\dot{\rho}_t - S(\omega_{i,t}^t)^2\rho_t. \tag{44}$$

Furthermore, the second term of Eq. (42), namely $-R_c^t S(R_t^c\dot{\omega}_{i,t}^t)\rho$, can be similarly manipulated. By applying **Lemma 2** to rearrange the rotation matrix and utilizing the definition $\rho_t = R_c^t\rho$, it simplifies directly to $-S(\dot{\omega}_{i,t}^t)\rho_t$. By recursively applying the relative kinematics and **Lemma 2** to eliminate intermediate frame transformations as demonstrated above, the remaining terms consolidate. Following this extensive algebraic simplification, the second time derivative of the relative position vector with respect to the target frame reduces to the following compact form:

$$\ddot{\rho}_t = -2S(\omega_{i,t}^t)\dot{\rho}t - S(\omega_{i,t}^t)^2\rho_t - S(\dot{\omega}_{i,t}^t)\rho_t + R_c^t\left(-\frac{\mu}{\|r_c\|^3}r_c - R_t^c\dot{v}_t + \frac{F}{m_c}\right). \tag{45}$$

Equation (45) explicitly reveals the affine relationship with respect to the actual control input F, allowing the dynamic HOCBF constraint to be directly integrated into a QP framework.

Acknowledgments

This work was supported by Korea Research Institute for defense Technology planning and advancement (KRIT) grant funded by the Korea government (DAPA (Defense Acquisition Program Adminis-

tration)) (No. KRIT-CT-22-030, Reusable Unmanned Space Vehicle Research Center, 2026) and by the Korea Agency for Infrastructure Technology Advancement (KAIA) grant funded by the Ministry of Land, Infrastructure and Transport (Grant RS-2026-25521384).

Declaration of Use of Artificial Intelligence

During the preparation of this manuscript, the authors utilized Artificial Intelligence (AI) tools in strict accordance with the conference's AI policy to assist with language refinement and programming productivity. Specifically, **Google Gemini 3.1 Pro** was employed for simple English proofreading and translation to improve the readability of the text. The authors carefully reviewed, corrected, and revised all language suggestions to ensure that the scientific integrity, underlying ideas, and authorship remain their own.

Furthermore, **Google Gemini 3.1 Pro** and the built-in AI assistant in **MATLAB R2025a** were utilized to assist with coding and algorithmic troubleshooting. These tools were specifically applied to the following two aspects of the research:

1) Assisting in the development of MATLAB scripts to generate a visualization figure that illustrates the reference frames defined prior to the equations of relative motion dynamics.
2) Exploring the theoretical causes and potential numerical solutions for an unbounded problem (specifically, `exitflag -3`) encountered in the Quadratic Programming (QP) solver during the Control Barrier Function formulation.

All AI-assisted codes, and generated outputs were rigorously verified, tested, and integrated by the authors. No AI tools were used to generate the core literature review, conclusions, or artwork autonomously. The authors ultimately take full responsibility and accountability for the correctness of the content, the scientific results, and the overall integrity of this work.

References

[1] Kim P Wabersich, Andrew J Taylor, Jason J Choi, Koushil Sreenath, Claire J Tomlin, Aaron D Ames, and Melanie N Zeilinger. Data-driven safety filters: Hamilton-jacobi reachability, control barrier functions, and predictive methods for uncertain systems. *IEEE Control Systems Magazine*, 43(5):137–177, 2023.

[2] Max H Cohen, Tamas G Molnar, and Aaron D Ames. Safety-critical control for autonomous systems: Control barrier functions via reduced-order models. *Annual Reviews in Control*, 57:100947, 2024.

[3] Shengbo Wang and Shiping Wen. Safe control against uncertainty: A comprehensive review of control barrier function strategies. *IEEE Systems, Man, and Cybernetics Magazine*, 11(1):34–47, 2025.

[4] Feng Zhang and Guangren Duan. Coupled dynamics and integrated control for position and attitude motions of spacecraft: A survey. *IEEE/CAA journal of Automatica sinica*, 10(12):2187–2208, 2023.

[5] Xiaodong Shao and Qinglei Hu. Immersion and invariance adaptive pose control for spacecraft proximity operations under kinematic and dynamic constraints. *IEEE Transactions on Aerospace and Electronic Systems*, 57(4):2183–2200, 2021.

[6] Liangyue Wang, Yanning Guo, Guangfu Ma, and Haibo Zhang. Artificial potential function based spacecraft proximity maneuver 6-dof control under multiple pyramid-type constraints. *ISA transactions*, 126:316–325, 2022.

[7] Yi Huang and Yingmin Jia. Adaptive finite-time 6-dof tracking control for spacecraft fly around with input saturation and state constraints. *IEEE Transactions on Aerospace and Electronic Systems*, 55(6):3259–3272, 2019.

[8] Liang Sun. Saturated adaptive output-constrained control of cooperative spacecraft rendezvous and docking. *IEEE/CAA Journal of Automatica Sinica*, 6(6):1462–1470, 2019.

[9] Liang Sun and Jingjing Jiang. Adaptive control of space proximity missions with constrained relative states, faults and saturation. *Acta Astronautica*, 174:211–218, 2020.

[10] Ding Zhou, Yanquan Zhang, and Shunli Li. Receding horizon guidance and control using sequential convex programming for spacecraft 6-dof close proximity. *Aerospace Science and Technology*, 87:459–477, 2019.

[11] Kai-Chieh Hsu, Haimin Hu, and Jaime F Fisac. The safety filter: A unified view of safety-critical control in autonomous systems. *Annual Review of Control, Robotics, and Autonomous Systems*, 7, 2023.

[12] Aaron D Ames, Samuel Coogan, Magnus Egerstedt, Gennaro Notomista, Koushil Sreenath, and Paulo Tabuada. Control barrier functions: Theory and applications. In *2019 18th European control conference (ECC)*, pages 3420–3431. Ieee, 2019.

[13] Wei Xiao and Calin Belta. High-order control barrier functions. *IEEE Transactions on Automatic Control*, 67(7):3655–3662, 2021.

[14] Qi Li, Bo Zhang, Jianping Yuan, and Huan Wang. Potential function based robust safety control for spacecraft rendezvous and proximity operations under path constraint. *Advances in Space Research*, 62(9):2586–2598, 2018.

[15] Quan Nguyen and Koushil Sreenath. Exponential control barrier functions for enforcing high relative-degree safety-critical constraints. In *2016 American Control Conference (ACC)*, pages 322–328. IEEE, 2016.

[16] Hanspeter Schaub and John L Junkins. *Analytical mechanics of space systems*. Aiaa, 2003.

[17] Rune Schlanbusch, Raymond Kristiansen, and Per J Nicklasson. Spacecraft formation reconfiguration with collision avoidance. *Automatica*, 47(7):1443–1449, 2011.